

A High-order Gas-Kinetic Navier-Stokes Solver I: One-dimensional Flux Evaluation

Qibing Li*

Department of Engineering Mechanics
Tsinghua University, Beijing 100084, P.R. China

Kun Xu†

Mathematics Department
Hong Kong University of Science and Technology, Hong Kong

Abstract

The foundation for the development of modern compressible flow solver is the Riemann solution of the inviscid Euler equations. The high-order schemes are basically related to high-order spatial interpolation or reconstruction. Due to the first-order wave interaction in the Riemann solution, the temporal accuracy is improved through the Runge-Kutta method, where the dynamic deficiencies in the 1st-order Riemann solution is alleviated through the sub-step spatial reconstruction in the Runge-Kutta process. The close coupling between the spatial and temporal evolution in the original nonlinear governing equations seems weakened due to its spatial and temporal decoupling. A solution under piecewise discontinuous high-order initial reconstruction for the Navier-Stokes equations directly is on a urgent need for many high-order methods. Unfortunately, the piece-wise discontinuous initial data and the hyperbolic-parabolic nature of the Navier-Stokes equations seem to be inconsistent mathematically, such as the divergence of the viscous and heat flux due to discontinuity. In this paper, based on the Boltzmann equation, we are going to present a flux function for the Navier-Stokes equations starting from a high-order reconstruction. The theoretical validity for such an approach is due to the fact that the Boltzmann equation has no specific requirement on the smoothness of the initial data and the kinetic equation has the mechanism to describe the gas evolution starting from an initial discontinuous data. The current high-order flux evaluation method is an extension of the second-order gas-kinetic BGK scheme for the Navier-Stokes equations (BGK-NS). The novelty for the easy extension from a 2nd-order, which is equivalent to the Generalized Navier-Stokes flow solver, to an even higher order is solely due to the simple particle transport mechanism on the microscopic level, i.e., the particle free transport and collisions. This paper will present a hierarchy to construct such a high-order method. Numerical examples for a 3rd-order scheme will be presented. The necessity to couple spatial and temporal evolution nonlinearly in the flux evaluation can be clearly observed through the numerical performance of the scheme for the viscous flow computations.

*email:lqb@tsinghua.edu.cn

†email:makxu@ust.hk

1 Introduction

The need for high-order numerical methods for the Navier-Stokes equations has been widely recognized in engineering applications, such as vortex-dominated flows, aeroacoustic noise predictions, LES/DNS computations for complex configurations. The current existing and popular high-order methods include the Essential Non-Oscillatory (ENO) [6], Weighted Essential Non-Oscillatory (WENO) [9], Discontinuous Galerkin (DG) [19, 2], Spectral Difference (SD) [14], Spectral Volume (SV) methods [23], Arbitrary accuracy DERivative (ADER) Riemann problem [21], compact schemes [3, 18], multi-moment constrained finite volume (MCV) method [7], and many others. Among these high-order methods, DG, SV, SD, and MCV methods are similar in the way that they share the same solution space, i.e., the space of piece-wise discontinuous polynomials, and a 1st-order Riemann solution is used at the element interface to provide solution for information exchange across discontinuous elements and appropriate numerical dissipation necessary to achieve stability. For ADER method, the main part is still the 1st-order Riemann solution and approximate linear equations are solved for high-order terms.

For high-order schemes, such as ENO, WENO, DG, SV, and SD methods, a high-order polynomial reconstruction (updated or interpolated) is obtained within each element or control volume. The physics of wave propagation starting from the high-order initial condition around the cell interface is accounted for through the Riemann solver, where two constant states are used for the flux evaluation [4, 20]. Even with the high-order spatial reconstruction, the physical evolution process from the initial data is basically coming from a first-order physical mechanism. This is probably the main reason for any high-order scheme the simulation results are sensitive to the limiters or reconstruction methods used. For example, many detectors, such as Harten's [5], Jameson's [8], and WENOs [9], have been invented to construct the point-wise values at the cell interfaces. In some flow problems, such as shock boundary interactions, the solution seems to be extremely sensitive to the detector used [18].

For the Navier-Stokes equations, the situation becomes even worse due to the hyperbolic-parabolic nature of the governing equations and the discontinuities in the reconstructed data. Certainly, the use of Runge-Kutta method helps for the improvement of time accuracy, but intrinsic nonlinear coupling in space and time in the gas evolution process seems get weakened. Physically, a solution should be one emerged directly from the discontinuous polynomials. If the whole curves on both sides of a discontinuity can be taken into account in the gas evolution process, the numerical solution will not be so sensitive to the point-wise values. So, in order to construct a high-order scheme, the development of a high-order NS flux function directly from a generalized discontinuous initial condition is important and preferable. Theoretically, the NS equations are coming from a model on the macroscopic scale and they require smooth flow distributions. But, due to the numerical side-effect, such as the cell resolution is not enough to resolve the physical structure, a discontinuity at the cell interface is artificially created. With the discontinuity initial condition, the Navier-Stokes formulations have severe difficulties mathematically due to the assumption of continuous function associated with the dissipative terms. So, a natural remedy for this in the current CFD community is to detect the shock discontinuity in the initial reconstruction scheme, then, one-sided finite differences for the shock point and high order central finite differences for the smooth part are basically used. But, to get a reliable detector or limiter in multidimensional case is not an easy task.

Based on the gas-kinetic theory, the Navier-Stokes equations can be derived from the Boltzmann equation using the Chapman-Enskog expansion. Theoretically, a Navier-Stokes solver can be obtained also by solving the Boltzmann equation, or a simplified kinetic collision model. However, the kinetic equation doesn't require any smoothness or continuity in its initial gas distribution.

So, it naturally fits with the high-order piece-wise discontinuous initial data of a high-order reconstruction. Therefore, the initial piece-wise discontinuity polynomials for the flow variables may be inconsistent with the underlying modeling of the Navier-Stokes equations, but they are perfectly acceptable for the Boltzmann equation.

In a gas-kinetic representation, all flow variables are moments of a single particle distribution function. Since a gas distribution function contains both equilibrium and nonequilibrium flow properties of the gas flow, the inviscid and viscous terms are obtained simultaneously. In the past years, a BGK-NS method based on the gas-kinetic BGK model [1] has been developed for the Navier-Stokes solutions under the linear polynomials for the mass, momentum, and energy distributions separated by a discontinuity at the origin [25]. The BGK-NS method has been successfully applied in many engineering applications, especially for the hypersonic viscous and heat conducting flows [27, 11, 12]. An attempt to develop a higher-order gas-kinetic scheme has been made for smooth flow [13]. This paper concerns with the construction of a general 3rd-order gas-kinetic flux function for the Navier-Stokes equations. Instead of using piece-wise linear distributions, initial data consist of two smooth parabolic curves for the conservative variables separated with a discontinuity at the origin. The generalization of the current methodology to arbitrary piecewise smooth curves can be done similarly. The possibility to construct such a method is mainly due to the simple particle transport mechanism in the microscopic level, i.e., free transport and collisions. The initial discontinuity jump and the ratio between time interval and particle collision time determine the emerging of wave patterns associated with the NS solutions. The high-order gas-kinetic scheme presented in this paper provides a valuable NS flux function, which can be implemented to many high-order fluid dynamic methods.

The paper is arranged in the following. Section 2 is about the construction of the 3rd-order gas-kinetic Navier-Stokes flux function under piece-wise discontinuous parabolic flow distributions. Section 3 is the analysis of the scheme and introduces its possible generalization to multiple dimensions. Section 4 is the numerical examples which illustrate the importance to develop a high-order flux function. Last section is the conclusion.

2 A high-order gas-kinetic Navier-Stokes flow solver

The focus of this section is to present a Navier-Stokes flux function under the generalized initial data by solving the gas-kinetic BGK equation, the so-called High-order BGK (HBGK) scheme.

2.1 High-order initial data reconstruction

Any high-order initial reconstruction, such as ENO, WENO, or DG methods can be used to obtain the subcell polynomials for the mass, momentum and energy distributions. For the conservative flow variables in one-dimensional case,

$$W = (\rho, \rho U, \rho E)^T,$$

the reconstructed data are

$$(1) \quad W(x, 0) = \begin{cases} W_L + \left(\frac{\partial W_L}{\partial x}\right)x + \frac{1}{2}\left(\frac{\partial^2 W_L}{\partial x^2}\right)x^2, & x < 0, \\ W_R + \left(\frac{\partial W_R}{\partial x}\right)x + \frac{1}{2}\left(\frac{\partial^2 W_R}{\partial x^2}\right)x^2, & x \geq 0, \end{cases}$$

where $x = 0$ is the cell interface. The focus of this paper is to construct a time-dependent flux function underlying the above initial condition. The reconstruction method used in this paper

is the parameter-free generalized moment (PFGM) limiter method [28]. Inside each cell i , the conservative variables are reconstructed as

$$(2) \quad W_i(x) = \bar{W}_i^{(0)} + \bar{W}_i^{(1)}(x - x_i) + \frac{1}{2}\bar{W}_i^{(2)}[(x - x_i)^2 - \frac{1}{12}h^2],$$

where h is the cell size and the coefficients

$$\begin{aligned} \bar{W}_i^{(0)} &= \bar{W}_i, \\ \bar{W}_i^{(1)} &= (\bar{W}_{i+1} - \bar{W}_{i-1})/2h, \end{aligned}$$

and

$$\bar{W}_i^{(2)} = (\bar{W}_{i+1} - 2\bar{W}_i + \bar{W}_{i-1})/h^2,$$

with cell averaged conservative variables \bar{W}_{i-1} , \bar{W}_i and \bar{W}_{i+1} in $(i-1)th$, ith and $(i+1)th$ cells. The above cell-averaged derivatives are limited in a hierarchical manner using a minmod-type limiter. Starting from the highest order derivatives, $\bar{W}_i^{(p)}$ is limited using

$$(3) \quad \bar{Y}_i^{(p)} = \min \text{ mod} \left(\bar{W}_i^{(p)}, 1.5 \frac{\bar{W}_{i+1}^{(p-1)} - \bar{W}_i^{(p-1)}}{h}, 1.5 \frac{\bar{W}_i^{(p-1)} - \bar{W}_{i-1}^{(p-1)}}{h} \right).$$

If $\bar{Y}_i^{(p)} = \bar{W}_i^{(p)}$, the highest derivative is not altered. No further limiting is required, and the solution remains the same. Otherwise, the limiting process proceeds to the next lower derivative in a similar fashion. Finally, the limited polynomial inside each cell is written

$$(4) \quad W_i(x) = \bar{Y}_i^{(0)} + \bar{Y}_i^{(1)}(x - x_i) + \frac{1}{2}\bar{Y}_i^{(2)}[(x - x_i)^2 - \frac{1}{12}h^2],$$

which is the basic reconstruction used in this paper. The above reconstruction, i.e., $\bar{W}^{(p)}$, is based on standard central difference methods, which are applied to all conservative variables in this paper. The order of the reconstruction is defined by the highest derivatives included, i.e., $p = 3$ means 3rd-order reconstruction and $p = 2$ is the 2nd-order one. The reconstruction of the polynomial is basically different from the order of the flux evaluation scheme. For example, the time-dependent flux in the 2nd-order BGK-NS scheme [25] is based on the evolution of linearly distributed mass, momentum and energy. But, a high-order reconstruction method can be still used to get the linear slopes, such as BGK-NS method with $p = 3$ reconstruction.

2.2 BGK Model and Viscous Equations

The one-dimensional BGK equation can be written as [1]

$$(5) \quad f_t + uf_x = \frac{g - f}{\tau},$$

where f is the gas distribution function and g is the equilibrium state approached by f . Both f and g are functions of space x , time t , particle velocities u , and internal variable ξ . The particle collision time τ is related to the viscosity and heat conduction coefficients. The equilibrium state is a Maxwellian distribution,

$$g = \rho \left(\frac{\lambda}{\pi} \right)^{\frac{K+1}{2}} e^{-\lambda((u-U)^2 + \xi^2)},$$

where ρ is the density, U is the macroscopic velocity in the x direction, and λ is equal to $m/2kT$, m is the molecular mass, k is the Boltzmann constant, and T is the temperature. For a 1D flow,

the total number of degrees of freedom K in ξ is equal to $(3 - \gamma)/(\gamma - 1)$ [25]. For example, for a diatomic gas with $\gamma = 7/5$, K is equal to 4 to account for the particle motion in the y and z -directions, as well as two rotational degrees of freedom. In the equilibrium state, the internal variable ξ^2 is equal to $\xi^2 = \xi_1^2 + \xi_2^2 + \dots + \xi_K^2$. The relation between mass ρ , momentum ρU , and energy ρE densities with the distribution function f is

$$(6) \quad \begin{pmatrix} \rho \\ \rho U \\ \rho E \end{pmatrix} = \int \psi_\alpha f d\Xi, \quad \alpha = 1, 2, 3,$$

where ψ_α is the component of the vector of moments

$$\boldsymbol{\psi} = (\psi_1, \psi_2, \psi_3)^T = (1, u, \frac{1}{2}(u^2 + \xi^2))^T,$$

and $d\Xi = dud\xi_1 d\xi_2 \dots d\xi_K$ is the volume element in the phase space with $d\xi = d\xi_1 d\xi_2 \dots d\xi_K$. Since mass, momentum, and energy are conserved during particle collisions, f and g satisfy the conservation constraint,

$$(7) \quad \int (g - f) \psi_\alpha d\Xi = 0, \quad \alpha = 1, 2, 3,$$

at any point in space and time.

Based on the above BGK model and the Chapman-Enskog expansion up to the Navier-Stokes order, i.e., $f = g - \tau(g_t + ug_x)$, the Navier-Stokes equations can be derived [17],

$$\begin{pmatrix} \rho \\ \rho U \\ E \end{pmatrix}_t + \begin{pmatrix} \rho U \\ \rho U^2 + p \\ (E + p)U \end{pmatrix}_x = \begin{pmatrix} 0 \\ \frac{2K}{K+1} \tau p U_x \\ \frac{K+3}{4} \tau p (\frac{1}{\lambda})_x + \frac{2K}{K+1} \tau p U U_x \end{pmatrix}_x,$$

where $\mu = \tau p$ is the dynamical viscosity coefficient. With the relation $\lambda = m/2kT$ and $C_p = 5k/2m$ for a monatomic gas, the heat conduction coefficient in the above equations becomes $\kappa = 5k\mu/2m$, and the Prandtl number becomes fixed with the value $Pr = \mu C_p / \kappa = 1$. This is a well known result for the BGK model. Numerically, since the heat flux can be explicitly evaluated at the cell interface, the energy flux can be slightly modified in the current method to simulate flows with any Prandtl number [25]. In the process of deriving Navier-Stokes equations, the Chapman-Enskog expansion requires the continuity and smoothness of the macroscopic flow variables. However, for the kinetic equation (5) itself, this requirement is not necessary. Therefore, under the initial piece-wise discontinuous polynomial, the kinetic equation has a wider applicable regime than the Navier-Stokes equations.

Different from the previous BGK-NS flow solver based on the linear polynomial expansion of the conservative variables on both sides of a cell interface [25], this paper will target on the numerical NS solutions under the parabolic polynomial expansions (1). To further extend the current method to higher order polynomials is straightforward.

2.3 High-order BGK flow solver

The general solution f of the BGK model (5) at a cell interface $x_{j+1/2}$ and time t is

$$(8) \quad f(x_{j+1/2}, t, u, \xi) = \frac{1}{\tau} \int_0^t g(x', t', u, \xi) e^{-(t-t')/\tau} dt' + e^{-t/\tau} f_0(x_{j+1/2} - ut),$$

where $x' = x_{j+1/2} - u(t - t')$ is the particle trajectory and f_0 is the initial gas distribution function f at the beginning of each time step ($t = 0$). Two unknowns g and f_0 must be specified in Eq.(8)

in order to obtain the solution f . In order to simplify the notation, $x_{j+1/2} = 0$ will be used in the following text.

In previous BGK-NS scheme [25, 11], based on the initial macroscopic variables, the initial gas distribution function f_0 is constructed as

$$(9) \quad f_0 = \begin{cases} g^l [1 + a^l x - \tau(a^l u + A^l)], & x < 0, \\ g^r [1 + a^r x - \tau(a^r u + A^r)], & x \geq 0, \end{cases}$$

where g^l and g^r are the Maxwellian distributions at the left and right hand sides of the cell interface, a and A are associated with its spatial and temporal derivatives of an equilibrium state. The non-equilibrium parts satisfy the compatibility condition,

$$(10) \quad \begin{aligned} \int (a^l u + A^l) \psi g^l d\Xi &= 0, \\ \int (a^r u + A^r) \psi g^r d\Xi &= 0. \end{aligned}$$

In the previous high-order DG-BGK schemes, even with high-order reconstruction, only linear slopes consistent with the above formulation are kept in the flux evaluation [15, 16], and the Runge-Kutta methods are used for the time accuracy. Although the previous high-order kinetic method has a consistent 3rd-order accuracy to certain standard test cases, the scheme is not a fully nonlinear method coupling spatial and temporal evolution from a high-order polynomial discontinuity.

In this paper, we are going to design a high-order BGK (HBGK) scheme which presents a time dependent flux function directly from a discontinuous parabolic macroscopic flow distributions. For this HBGK scheme, the initial reconstruction of the conservative variables include 2nd-order derivatives. First, based on the high-order polynomial reconstruction presented in the subsection (2.1), we need to evaluate the corresponding Chapman-Enskog distribution function for the Navier-Stokes equations on both sides of a cell interface. The Chapman-Enskog expansion of the kinetic equation to the Navier-Stokes order is,

$$f_{NS}(0, 0) = g(1 - \tau(au + A)),$$

where g is the equilibrium state,

$$a = (\partial g / \partial x) / g = a_1 + a_2 u + a_3(u^2 + \xi^2),$$

and

$$A = (\partial g / \partial t) / g = A_1 + A_2 u + A_3(u^2 + \xi^2).$$

With a second-order initial polynomial distribution, the above NS distribution function can be expanded as

$$(11) \quad \begin{aligned} f_{NS}(x, 0) &= f_{NS}(0, 0) + \frac{\partial f_{NS}}{\partial x} x + \frac{1}{2} \frac{\partial^2 f_{NS}}{\partial x^2} x^2 \\ &= g \left[1 - \tau(au + A) + ax - \tau(C + aA)x + (a^2 + b)(-\tau ux + \frac{1}{2}x^2) \right], \end{aligned}$$

where $b = \partial a / \partial x$ and $C = \partial A / \partial x$. Therefore, with the initial discontinuous reconstruction (1), the corresponding NS non-equilibrium states on both sides of a cell interface can be constructed,

$$(12) f_0 = \begin{cases} g^l \left[1 - \tau(a^l u + A^l) + a^l x - \tau(C^l + a^l A^l)x + ((a^l)^2 + b^l)(-\tau ux + \frac{1}{2}x^2) \right], & x < 0 \\ g^r \left[1 - \tau(a^r u + A^r) + a^r x - \tau(C^r + a^r A^r)x + ((a^r)^2 + b^r)(-\tau ux + \frac{1}{2}x^2) \right], & x \geq 0 \end{cases},$$

where all parameters are determined through the following relations, see figure 1. First, let's define some notation for the moments of the equilibriums states,

$$\langle \dots \rangle_l = \int_{-\infty}^{\infty} g^l(\dots) \psi d\Xi, \quad \langle \dots \rangle_r = \int_{-\infty}^{\infty} g^r(\dots) \psi d\Xi,$$

and

$$\langle \dots \rangle_l|_{u>0} = \int_0^{\infty} g^l(\dots) \psi d\Xi, \quad \langle \dots \rangle_r|_{u<0} = \int_{-\infty}^0 g^r(\dots) \psi d\Xi.$$

The equilibrium states g^l and g^r are obtained from macroscopic pointwise values at the cell interface,

$$\int g^l \psi d\Xi = W_L, \quad \int g^r \psi d\Xi = W_R.$$

Then, parameters a and b in f_0 are determined using the slopes of macroscopic variables on the left and right hand sides separately,

$$\begin{aligned} \langle a^l \rangle_l &= \partial W_L / \partial x, & \langle a^r \rangle_r &= \partial W_R / \partial x, \\ \langle (a^l)^2 + b^l \rangle_l &= \partial^2 W_L / \partial x^2, & \langle (a^r)^2 + b^r \rangle_r &= \partial^2 W_R / \partial x^2. \end{aligned}$$

Based on the compatibility condition (7), other parameters can be determined as

$$\begin{aligned} \langle A^l + a^l u \rangle_l &= 0, & \langle A^r + a^r u \rangle_r &= 0, \\ \langle C^l + a^l A^l + ((a^l)^2 + b^l) u \rangle_l &= 0, & \langle C^r + a^r A^r + ((a^r)^2 + b^r) u \rangle_r &= 0. \end{aligned}$$

After having f_0 , the equilibrium state g_0 around $(x = 0, t = 0)$ can be constructed with spatial and temporal accuracy consistent with f_0 ,

$$\begin{aligned} g(x, t) &= g_0 + \frac{\partial g_0}{\partial x} x + \frac{\partial g_0}{\partial t} t + \frac{1}{2} \frac{\partial^2 g_0}{\partial x^2} x^2 + \frac{1}{2} \frac{\partial^2 g_0}{\partial t^2} t^2 + \frac{\partial^2 g_0}{\partial x \partial t} x t \\ (13) \quad &= g_0 \left[1 + ax + At + \frac{1}{2}(a^2 + b)x^2 + \frac{1}{2}(A^2 + B')t^2 + (C + aA)xt \right], \end{aligned}$$

where g_0, a, A, B', C will be determined later using the compatibility condition between f and g . Here, g_0 is a local Maxwellian distribution function located at the cell interface, see figure 1.

Let's first determine g_0 at $(x = 0, t = 0)$, i.e.,

$$g_0 = \rho_0 \left(\frac{\lambda_0}{\pi} \right)^{\frac{K+1}{2}} e^{-\lambda_0((u-U_0)^2 + \xi^2)}.$$

Taking the limit $t \rightarrow 0$ in Eq.(8) and substituting its solution into Eq.(7), the conservation constraint at $(x = 0, t = 0)$ gives

$$(14) \quad \int g_0 \psi d\Xi = W_0 = \int_{u>0} \int g^l \psi d\Xi + \int_{u<0} \int g^r \psi d\Xi,$$

where $W_0 = (\rho_0, \rho_0 U_0, \rho_0 E_0)^T$ is the macroscopic conservative flow variables located at the cell interface at time $t = 0$. Since g^l and g^r have been obtained earlier, the above moments can be evaluated explicitly. Therefore, the conservative variables $\rho_0, \rho_0 U_0$, and $\rho_0 E_0$ at the cell interface can be obtained, from which g_0 is uniquely determined. For example, λ_0 in g_0 can be found from

$$\lambda_0 = (K + 1) \rho_0 / (4(\rho_0 E_0 - \frac{1}{2} \rho_0 U_0^2)).$$

Based on the conservative variables W_0 at the cell interface $x = 0$, and the cell averaged values \bar{W}_j and \bar{W}_{j+1} on the left and right hand sides, the three conditions uniquely determine a continuous flow distributions at $t = 0$,

$$W(x, 0) = W_0 + \frac{\partial W_0}{\partial x}x + \frac{1}{2} \frac{\partial^2 W_0}{\partial x^2}x^2,$$

from which the equilibrium gas distribution functions in Eq.(13) at $t = 0$ can be obtained. With the definition

$$\langle \dots \rangle = \int_{-\infty}^{\infty} g_0(\dots)\psi d\Xi,$$

the corresponding terms in the distribution g in Eq.(13) can be obtained in the following,

$$\langle a \rangle = \frac{\partial W_0}{\partial x},$$

and

$$\langle b + a^2 \rangle = \frac{\partial^2 W_0}{\partial x^2}.$$

Before further determining A, B' , and C in $g(x, t)$, let's first substitute Eq.(12) and Eq.(13) into Eq.(8), the gas distribution function f at a cell interface can be expressed as

$$\begin{aligned} f(x_{j+1/2}, t, u, v, \xi) &= (1 - e^{-t/\tau}) g_0 \\ &+ (-\tau + (\tau + t)e^{-t/\tau}) a u g_0 \\ &+ (t - \tau + \tau e^{-t/\tau}) A g_0 \\ &+ (2\tau^2 - (t^2 + 2\tau t + 2\tau^2)e^{-t/\tau}) (a^2 + b) u^2 g_0 \\ &+ (t^2/2 - \tau t + \tau^2 - \tau^2 e^{-t/\tau}) (A^2 + B') g_0 \\ &+ (2\tau^2 - \tau t - (2\tau^2 + \tau t)e^{-t/\tau}) (C + aA) u g_0 \\ &+ e^{-t/\tau} \left(1 - \tau(a^l u + A^l) - a^l u t + \tau t(C^l + a^l A^l) u \right. \\ &\quad \left. + (\tau t + \frac{1}{2}t^2)((a^l)^2 + b^l) u^2 \right) \text{H}(u) g^l \\ &+ e^{-t/\tau} \left(1 - \tau(a^r u + A^r) - a^r u t + \tau t(C^r + a^r A^r) u \right. \\ &\quad \left. + (\tau t + \frac{1}{2}t^2)((a^r)^2 + b^r) u^2 \right) (1 - \text{H}(u)) g^r. \end{aligned} \tag{15}$$

The unknowns left in the above expression are A, B' and C . Here we use the following simple method to determine them,

$$\begin{aligned} \langle A + a u \rangle &= 0, \\ \langle C + A a + (a^2 + b) u \rangle &= 0, \\ \langle B' + A^2 + (C + A a) u \rangle &= 0. \end{aligned}$$

Finally, the time-dependent numerical fluxes in the x -direction across the cell interface can be computed as

$$\begin{pmatrix} \mathcal{F}_\rho \\ \mathcal{F}_{\rho U} \\ \mathcal{F}_{\rho E} \end{pmatrix}_{j+1/2} = \int u \begin{pmatrix} 1 \\ u \\ \frac{1}{2}(u^2 + \xi^2) \end{pmatrix} f(x_{j+1/2}, t, u, \xi) d\Xi, \tag{16}$$

where $f(x_{j+1/2}, t, u, \xi)$ is given in Eq.(15). By integrating the above equation to the whole time step, we can get the total mass, momentum and energy transport.

2.4 Boundary Conditions

For a high-order flow solver, the reconstruction requires high-order accurate boundary conditions. Here the second-order reconstruction is used to obtain the unknown variables at boundaries. For convenience, the ghost cell concept is adopted. For example, labeled as '-1' corresponding to the 1st cell inside the boundary. If the value of a variable at the boundary W_b is known (Dirichlet problem), its slope can be obtained through Taylor expansion,

$$(17) \quad W'_b = (-6W_b + 7\bar{W}_1 - \bar{W}_2)/2h.$$

Then the value for the ghost cell can be computed as

$$(18) \quad \bar{W}_{-1} = \bar{W}_1 - hW'_b, \quad \bar{W}_{-2} = \bar{W}_2 - 3hW'_b.$$

Another boundary value problem is that the slope W'_b is known (Neumann problem), then the ghost cell values can be directly calculated by the above formula. For viscous flow simulation, the wall boundary conditions can be set up through the combination of the above two types. For example, the non-slip adiabatic condition can be achieved using the first type of boundary condition for velocities and the second type for temperature and density. Higher order accurate boundary conditions can be constructed similarly with more ghost cells.

3 Analysis of high-order BGK (HBGK) scheme

In order to validate Eq.(15) as a correct Navier-Stokes flux function, let's consider the following limiting case. Eq.(15) gives explicitly the time-dependent gas distribution function f at the cell interface under discontinuous initial condition. In a well resolved flow region, such as the flow inside a resolved boundary layer, the reconstructed conservative variables will be a continuous one. In such a case, the distribution function f_0 has $g^l = g^r, a^l = a^r, A^l = A^r, C^l = C^r$, and $b^l = b^r$. Consequently, Eq.(14) gives $g_0 = g^l = g^r$, and thus $a = a^l = a^r, b = b^l = b^r$. Therefore, in the continuous case the gas distribution function f at a cell interface becomes

$$(19) \quad f_{NS} = g_0 \left[1 - \tau(ua + A) + tA - \tau t(aA + C)u + (-\tau t + \frac{1}{2}t^2)(A^2 + B') \right],$$

which exactly corresponds to a high-order Navier-Stokes gas distribution function in the smooth flow situation. If we compare the above equation with the BGK-Burnett solution [26, 17],

$$(20) \quad f_{Burnett} = g_0 \left[1 - \tau(ua + A) + tA + (2\tau^2 - \tau t)(C + aA)u + (\tau^2 - \tau t + \frac{1}{2}t^2)(A^2 + B') \right. \\ \left. + \tau^2(a^2 + b)u^2 + (\tau^2 - \tau t)B'' \right],$$

the Burnett solutions include more terms, such as those which are proportional to τ^2 ,

$$(21) \quad g_0 \left(2\tau^2(C + aA) + \tau^2(a^2 + b)u^2 + (\tau^2 - \tau t)B'' \right),$$

where B'' is obtained through the condition

$$\langle B'' + B' + A^2 + 2(C + aA)u + (a^2 + b)u^2 \rangle = 0.$$

So, it is interesting to observe that some terms in the Burnett expansion (20) are actually high-order Navier-Stokes terms due to the high-order spatial derivatives. In the gas-kinetic approach, the

second-order or higher-order spatial derivatives of flow variables can be used in the gas distribution function, subsequently effect the flux. The additional terms in (21) contained in the Burnett expansion contribute to the instability associated with the Burnett equations at high Mach number case. These terms related to high-order NS solutions do not contribute to the intrinsic instability of the Burnett solution for high frequency waves.

The piece-wise discontinuous initial data is solely due to the numerical requirement as the cell resolution is not enough to resolve the physical flow structure. The NS equations have intrinsic difficulties to cope with the discontinuities because of its continuous assumption for the flow variables in its modeling. Physically, the smoothness of flow variables can be only achieved in a time scale much larger than the particle collision time. So, it is invalid for the Navier-Stokes equations in a time scale of particle collision time τ or less after initial breaking down of the discontinuity in the gas evolution process. However, the gas-kinetic equation is valid in all time $t \geq 0$, and the solution from the initial breakdown of the discontinuity can be obtained from the BGK model. The kinetic flux function covers the particle free transport ($0 < t < \tau$), the transition regime ($\tau \approx t$), and the hydrodynamic regime ($\tau \ll t$). The difficulties associated with the NS equations are mainly due to the underlying physics of the governing equations, which is a modeling on the time scale $t \gg \tau$. It is also interesting to observe that in the continuous case for the high-order Navier-Stokes solution, there are no terms being proportional to τ^2 , which corresponding viscosity coefficient square. However, under the general discontinuous conditions, Eq.(15) clearly shows the terms related to τ^2 . This effect is also due to the initial discontinuity and the nonlinearity in the particle relaxation process. In summary, for polynomial distribution functions which are discontinuous at the origin, the Navier-Stokes formulation has no enough physical mechanism to handle the discontinuities.

In this paper, we only present the one-dimensional high-order kinetic flux function. However, this scheme can be naturally extended to 2D and 3D cases by developing a high-order multidimensional method using the methodology presented earlier [27, 10]. For example, based on the piece-wise polynomial in 3D case on the left and right hand sides of a cell interface,

$$\begin{aligned}
 W(x, y, z, 0) &= W_0 + (\partial W / \partial x)x + (\partial W / \partial y)y + (\partial W / \partial z)z \\
 &\quad + \frac{1}{2} \left((\partial^2 W / \partial x^2)x^2 + (\partial^2 W / \partial y^2)y^2 + (\partial^2 W / \partial z^2)z^2 \right) \\
 &\quad + \left((\partial^2 W / \partial x \partial y)xy + (\partial^2 W / \partial y \partial z)yz + (\partial^2 W / \partial z \partial x)zx \right) \\
 &\quad + \dots,
 \end{aligned}
 \tag{22}$$

a corresponding non-equilibrium high-order Navier-Stokes gas distribution function f_0 can be constructed. With the expansion of the equilibrium state g , the time evolution f can be obtained based on the integral solution of the BGK model. The scheme is multidimensional because all gradients normal and tangential to a cell surface will participate in the gas evolution process.

More importantly, in the continuum limit as the flow structure is well-resolved by the cell size, the discontinuities disappear at the cell interface. The above kinetic formulation with the explicit account of particle transport (or upwinding in CFD terminology) will go back to the traditional Chapmann-Enskog expansion for the continuum flow (corresponding to central-difference method in CFD community). Therefore, the multidimensional gas-kinetic scheme is a unification of upwinding and central difference schemes. So, it is not surprising that a high-order gas-kinetic scheme can be developed for the Navier-Stokes solutions under the piece-wise discontinuous initial data where the solutions have both hyperbolic (upwinding) and parabolic (central difference) nature.

4 Numerical experiments

Five cases are tested to validate the present high-order BGK (HBGK) method, from the Navier-Stokes shock structure to the Couette flow with a temperature gradient. In order to compare the previous 2nd-order BGK scheme, the results from the BGK-NS method is also included in certain cases. Unless otherwise stated, in all numerical examples reported here, a specific heat ratio $\gamma = 1.4$ and unity Prandtl number are adopted and the collision time is given by

$$(23) \quad \tau = \tau_m + \tau_a,$$

where the molecular viscosity is calculated by $\tau_m = \frac{\mu}{p}$ for viscous flow and $\tau_m = 0.01\Delta t$ for inviscid case. The second part for the collision time accounts for the artificial numerical viscosity and is chosen to be $\tau_a = 0.1 \frac{|p^l - p^r|}{|p^l + p^r|} \Delta t$. The computational time step Δt is determined by

$$(24) \quad \Delta t = \frac{C_{\Delta t} \Delta x}{|U| + a + 2\nu/\Delta x}$$

with the CFL number $C_{\Delta t} = 0.3$. The kinetic viscosity coefficient ν in the above formula is set to zero for inviscid flow. For simplicity, the uniform grid is used and the reconstruction is based on the third-order polynomial for the shock structure problem. For other cases, the second-order PFGM limiter [28] ($p = 2$) is used mostly for the direct reconstruction of conservative variables. Since we are emphasizing the construction of the Navier-Stokes flux function from a high-order polynomials in this paper, we do not intend to use different reconstruction schemes to improve the performance of individual test case.

Case (1) Navier-Stokes Shock Structure

The performance of the present scheme in viscous dominated smooth flow is tested in this case. The initial condition is set as a stationary shock with inflow Mach number $M = 1.1$, $\rho_1 = 1$, $U_1 = 1$ and $\gamma = 5/3$. The computational domain is chosen as $[-0.025, 0.025]$ according to the constant viscosity $\mu = 2.5 \times 10^{-4}$. To fix the location of the shock, the Dirichlet condition is adopted at the downstream boundary based on the analytic solution. For example, the velocity is set, $U = U_2 + 0.02(1 - U_2)$ at $x = 0.025$, where U_2 is post-shock velocity computed from Rankine-Hugoniot condition. Other unknowns are calculated through interpolation. The analytic solution is obtained by solving the ordinary differential equations [25].

Figure 2 shows the computed density distribution with different grid number. Good grid convergence is achieved and the NS shock structure can be satisfactorily captured even with only three grid points inside the shock ($N = 8$). The deviation from the analytic solution is shown in figure 3, where the error norm is calculated with grid points inside the shock layer ($0 \leq x \leq 0.025$). Third-order accuracy of the present scheme is confirmed.

Case (2) Blast Wave

The blast wave problem, originally proposed by Woodward and Colella [24], is simulated to evaluate the performance of the present high-order gas-kinetic BGK scheme for flow with very strong shocks and contact discontinuities. The computational domain is $[0, 1]$ with reflecting boundary condition on both sides. The initial flow field is stationary with unity density. The pressure is 1000 for $0 \leq x < 0.1$, 100 for $0.9 \leq x \leq 1$, and 0.01 between them.

Figure 4 and 5 show the computed density and pressure distributions at $t = 0.038$ with grid number $N = 800$, which are compared with the reference solution obtained by the original second-order BGK scheme with grid number $N = 10000$, where van Leer slope limiter is used in the 2nd-order method. We can observe that the strong shock and contact discontinuities, particularly for the local extrema are well resolved by the HBGK method.

Case (3) Shu-Osher Shock Acoustic-Wave Interaction

This problem is the interaction of a moving shock with smooth density fluctuations. The computational domain is $[-5, 5]$ and the flow field is initialized as,

$$(25) \quad (\rho, U, p) = \begin{cases} (3.857134, 2.629369, 10.33333), & x < -4 \\ (1 + 0.2 \sin(5x), 0, 1), & x \geq -4 \end{cases}.$$

The computed density profiles with grid number $N = 400$ at time $t = 1.8$ is shown in figure 6 and compared with the solid curve of a refined-mesh calculation. With the simple second-order PFGM limiter [28], both of the sharp shock discontinuity and acoustic oscillation are well captured. A close-up view of the acoustic region is shown in figure 7. It should be noted that the limiter applied in the reconstruction plays an important role in the performance of a scheme. For the original second-order gas-kinetic BGK scheme with the MUSCL limiter, the produced local extremes are not satisfactory. But if the 2nd-order BGK-NS scheme is combined with the PFGM limiter ($p=2$), it gives a much better solution, which is nearly identical to the present HBGK scheme. If we want to further improve the result, a high-order reconstruction may be a good choice. As shown in figure 8, with the help of the third-order PFGM limiter ($p = 3$), the local extreme, especially in the lower parts of oscillatory solution, is evidently better resolved with the present HBGK scheme. But the situation is not the same for the original second-order BGK method, which seems not benefit from the higher-order limiter. To achieve more accurate result, besides the well-tuned reconstruction method and limiter, the use of a high-order flux function is also important.

Case (4) Couette Flow with a Temperature Gradient

The Couette flow is another typical flow governed by the compressible NS equations with analytical solution. It is considered here to test the performance of the present HBGK scheme in viscous shear and heat conducting dominated flow. The flow is one-dimensional but with an additional velocity component V . Thus another freedom should be included in the gas distribution function.

The left wall is fixed and the right one is moving at a speed $V = 1$ in the vertical direction. The temperatures at the left and right are given by T_0 and T_1 . Under the assumption of constant viscosity $\mu = 5 \times 10^{-3}$ and heat conduction coefficients, a steady analytic temperature distribution can be deduced,

$$(26) \quad \frac{T - T_0}{T_1 - T_0} = \frac{x}{H} + \frac{\text{PrEc}}{2} \frac{x}{H} \left(1 - \frac{x}{H}\right),$$

where $H = 1$ is the height of the channel, Pr is the Prandtl number and Ec is the Eckert number $\text{Ec} = U^2 / C_p (T_1 - T_0)$. In the present study, $\text{Ec} = 20$ and a Mach number $M = 0.1$ are considered. The CFL number is set to be 0.6.

Figure 9 shows the computed temperature distributions with different grid numbers. Again it can be observed that good grid convergence is achieved and the temperature profile can be well captured even with only five grid points by the current HBGK method. That means the wall heat flux can be accurately predicted. The previous BGK scheme with PFGM limiter also works very well in this case (see figure 10). But the deviation is clearly observed when MUSCL limiter is adopted in the previous BGK scheme. This indicates the importance of high-accurate reconstruction, especially for viscosity dominated flow.

Case (5) Flow near an Oscillating Plate

The last test case is the low-speed flow near a vertically oscillating flat plate with infinite length. The flow is also dominated by the viscous shear, and the analytical solution can be derived from NS equation as,

$$(27) \quad V(x, t) = V_0 e^{-kx} \cos(\omega t - kx),$$

under the incompressible assumption and the boundary condition, $V(0, t) = V_0 \cos \omega t$, and $V(\infty, t) = 0$. Here $k = \sqrt{\omega/2\nu}$ is the wave number and ν is the kinetic viscosity coefficient. In the present study, we set the constants as, $V_0 = 1$, $\nu = 0.01$ and $\omega = 8\pi^2\nu$. Thus the wave length for the damping velocity is $\lambda_x = 2\pi/k = 1$. The computational domain is chosen as $[0, 3]$ divided by N uniform cells. The initial flow field is stationary with unity density and pressure $1/\gamma M^2$ with $\gamma = 5/3$ and Mach number $M = V_0/a = 0.1$. The non-slip adiabatic boundary condition at the plate is adopted. At the right boundary, the conservative variables are given based on the analytic solution. The CFL number is set to be 0.6.

Figure 11 shows the computed velocity distributions at time $t = 22.4$ and 24 with different grid numbers. Good grid convergence is achieved and the velocity profile can be satisfactorily captured even with only several grid points by the current HBGK method. Good performance of the previous 2nd-order BGK scheme with 2nd-order PFGM limiter is also validated in this case. As shown in figure 12, the BGK solution with 30 cells is identical to that computed by the present HBGK scheme and both show good agreement with the analytic one. However, when the flow is not well-resolved, such as $N = 15$, the HBGK scheme shows a little better performance than the 2nd-order BGK scheme. When the computational time step is larger, for example, when the CFL number is 0.9, the advantage becomes evident (see figure 13). This means that with the same reconstruction ($p = 2$), HBGK scheme can improve the accuracy because a large portion of reconstructed flow around the discontinuity will participate in the flux construction. On the contrary, for the Riemann solver only two point-wise values at the cell interface are used.

Overall, these test cases validate the good performance of the present high-order gas-kinetic BGK scheme, not only for the flow with discontinuity, but also for the smooth flow with viscosity dominated structure, such as the one inside a boundary layer.

5 Conclusion

In this paper, we present a high-order gas-kinetic scheme for the Navier-Stokes equations. The scheme provides a time-dependent Navier-Stokes flux function under the generalized piece-wise polynomials for the flow variables with a discontinuity at the origin. In the current high-order scheme, the high-order spatial and temporal derivatives are coupled nonlinearly in the gas evolution process. Due to the incorporation of the whole reconstructed curves into the flux evaluation, one obvious advantage of the current scheme is that its solution is not sensitive to the point-wise values at the interface, the so-called initial data for the Riemann problem. A multidimensional gas-kinetic method can be also constructed in 2D and 3D cases. The flux function provided in this paper can be used in many high-order methods, such as DG, SV, and SD, for the compressible Navier-Stokes solutions. The success of the gas-kinetic scheme is due to its simple particle transport mechanism, i.e., free transport and collision, underlying the kinetic equation. For the macroscopic equations, different types, i.e., parabolic and hyperbolic, seek different numerical treatments. The kinetic formulation has the mechanism to capture the particle relaxation process from a discontinuous initial data at any time $t > 0$, where the physical validity of the Navier-Stokes equations itself is valid on a time scale $t \gg \tau$. So, it is not surprising that there exist difficulties in many high-order methods for the Navier-Stokes solutions starting from a discontinuity. The use of the kinetic flux function is indispensable for the development of reliable high-order CFD methods.

Acknowledgments

This work is supported by National Natural Science Foundation of China (Project No. 10872112).

References

- [1] P.L. Bhatnagar, E.P. Gross, and M. Krook, *A Model for Collision Processes in Gases I: Small Amplitude Processes in Charged and Neutral One-Component Systems*, Phys. Rev., **94** (1954), pp. 511-525.
- [2] B. Cockburn, G.E. Karniadakis, C.W. Shu, *The development of discontinuous Galerkin methods*, Discontinuous Galerkin Methods, edited by B. Cockburn, G.E. Karniadakis, and C.W. Shu, Berlin: Springer (2000).
- [3] X.G. Deng and H.X. Zhang, *Developing High-Order Weighted Compact Nonlinear Schemes*, J. Comput. Phys., Volume **165** (2000), pp. 22-44.
- [4] S.K. Godunov, *A Difference Scheme for Numerical Computation of Discontinuous Solutions of Hydrodynamic Equations*, Math. Sbornik, **47** (1959), pp. 271.
- [5] A. Harten, *The artificial compression method for computation of shocks and contact discontinuities: III self-adjusting hybrid schemes*, Mathematics of Computation, Vol. **32** (1978), pp. 363-389.
- [6] A. Harten, B. Engquist, S. Osher, S. Chakravarthy, *Uniformly high-order essentially non-oscillatory schemes III*, J. Comput. Phys., **71** (1987), pp. 231-303.
- [7] S. Ii and F. Xiao, *High order multi-moment constrained finite volume method. Part I: basic formulation*, J. Comput. Phys., vol. **228** (2009), pp. 3669-3707.
- [8] A. Jameson, W. Schmidt, and E. Turkel, *Numerical solution of the Euler equations by finite volume methods using Runge-Kutta time stepping schemes*, AIAA paper 1981-1259 (1981).
- [9] G. Jiang and C.W. Shu, *Efficient implementation of weighted ENO schemes*, J. Comput. Phys., **126** (1996), pp. 202-228.
- [10] Q. Li and S. Fu, *On the multidimensional gas-kinetic BGK scheme*, J. Comput. Phys., vol. **220** (2006), pp. 532-548.
- [11] Q. Li, S. Fu, and K. Xu, *A compressible Navier-Stokes flow solver with scalar transport*, J. Comput. Phys., vol. **204** (2005), pp. 692-714.
- [12] Q.B. Li, S. Fu, and K. Xu, *Application of BGK scheme with kinetic boundary conditions in hypersonic flow*, AIAA J., vol. **43** (2005), pp. 2170-2176.
- [13] Q. Li and S. Fu, *A high-order accurate gas-kinetic BGK scheme*, 5th International Conference on Computational Fluid Dynamics, July 7-11, 2008, Seoul, Korea.
- [14] Y. Liu, M. Vinokur, and Z.J. Wang, *Discontinuous spectral difference method for conservation laws on unstructured grids*, J. Comput. Phys. **216** (2006), pp. 780-801.
- [15] H.W. Liu and K. Xu, *A Runge-Kutta Discontinuous Galerkin Method for Viscous Flow Equations*, J. Comput. Phys. **224** (2007), pp. 1223-1242.
- [16] H. Luo, L. Luo, and K. Xu, *A discontinuous Galerkin method based on a BGK scheme for the Navier-Stokes equations on arbitrary grids*, Adv. Appl. Math. Mech. **1** (2009), pp. 301-318.

- [17] T. Ohwada and K. Xu, *The kinetic scheme for full Burnett equations*, J. Comput. Phys., vol. **201** (2004), pp.315-332.
- [18] M. Oliveria, P. Liu, X. Liu, and C. Liu, *Universal high order subroutine with new shock detector for shock boundary layer interaction*, to appear in Int. J. Computer Mathematics (2009).
- [19] W.H. Reed and T.R. Hill, *Triangular mesh methods for the neutron transport equation*, Technical report LA-UR-73-479, Los Alamos Scientific Laboratory (1973).
- [20] E. Toro, *Riemann Solvers and Numerical Methods for Fluid Dynamics*, Springer (1999).
- [21] E. Toro, R.C. Millington, and L.A.M. Nejad, *Towards very high order Godunov schemes*, in: E.F. Toro (ed.), *Godunov Methods: Theory and Applications*, Kluwer/Plenum Academic Publishers (2001), pp. 907-940.
- [22] W.G. Vincenti and C.H. Kruger, Jr., *Introduction to Physical Gas Dynamics*, Wiley, New York (1965).
- [23] Z.J. Wang, *Spectral (finite) volume method for conservation laws on unstructured grids: basic formulation*, J. Comput. Phys., **178** (2002), pp. 210-251.
- [24] P. Woodward and P. Colella, *Numerical Simulations of Two-dimensional Fluid Flow with Strong Shocks*, J. Comput. Phys., **54** (1984), pp. 115.
- [25] K. Xu, *A Gas-kinetic BGK Scheme for the Navier-Stokes Equations, and Its Connection with Artificial Dissipation and Godunov Method*, J. Comput. Phys., Vol. **171** (2001), pp. 289-335.
- [26] K. Xu and Z.H. Li, *Microchannel flows in slip flow regime: BGK-Burnett solutions*, J. Fluid Mechanics (2004), vol. **513**, pp. 87-110
- [27] K. Xu, M.L. Mao, and L. Tang, *A multidimensional gas-kinetic BGK scheme for hypersonic viscous flow*, J. Comput. Phys., vol. **203** (2005), pp. 405-421.
- [28] M. Yang and Z.J. Wang, *A parameter-free generalized moment limiter for high-order methods on unstructured grids*, AIAA 2009-605, 47th AIAA Aerospace Sciences Meeting Including The New Horizons Forum and Aerospace Exposition, January 5-8, 2009, Orlando, Florida.

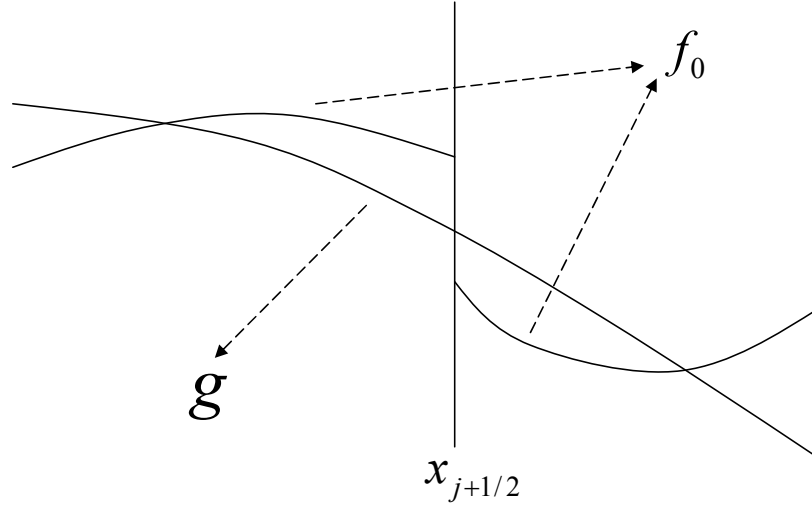


Figure 1: Equilibrium and non-equilibrium gas distribution functions across a cell interface.

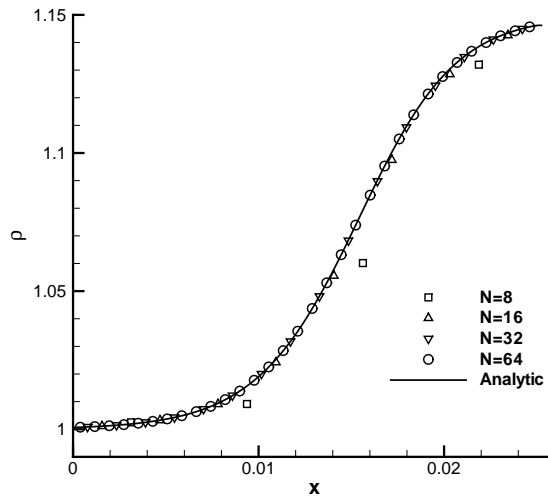


Figure 2: Density distribution inside a stationary shock from HBGK scheme.

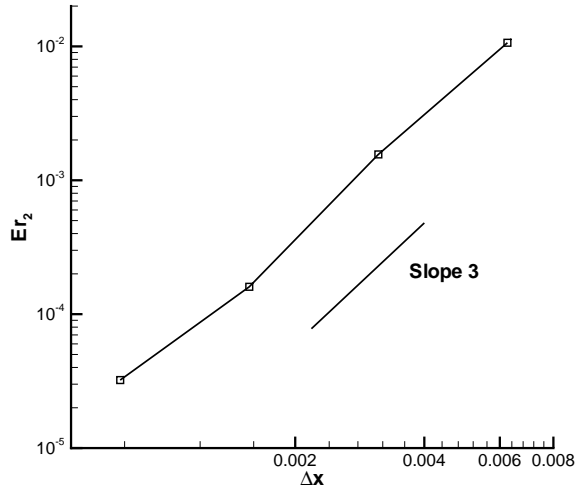


Figure 3: Variation of the second error norm with cell size for HBGK for shock structure problem.

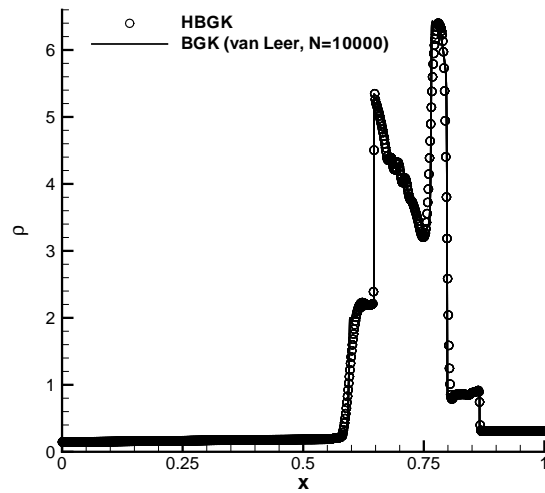


Figure 4: Density distribution for the Woodward and Colella problem from the current HBGK scheme with 800 points. The reference solution is obtained from 2nd-order BGK-NS method with 10000 points.

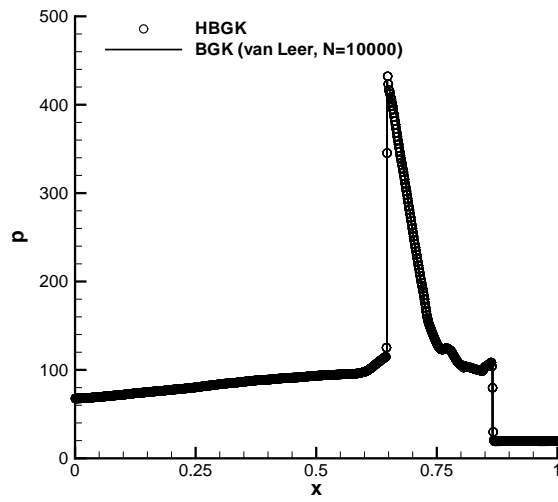


Figure 5: Pressure profiles for the Woodward and Colella problem.

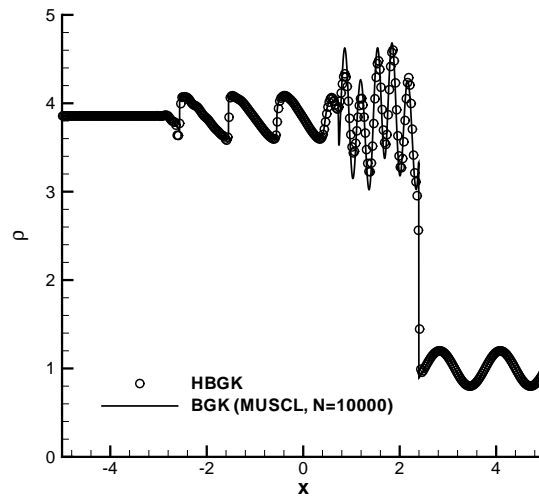


Figure 6: Density distributions for shock acoustic wave interaction from HBGK scheme.

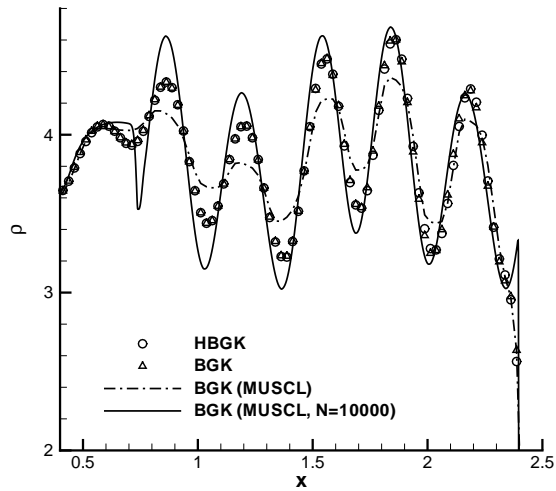


Figure 7: Detailed density distributions calculated by HBGK ($p=2$), previous 2nd-order BGK scheme ($p=2$), and BGK with MUSCL limiter.

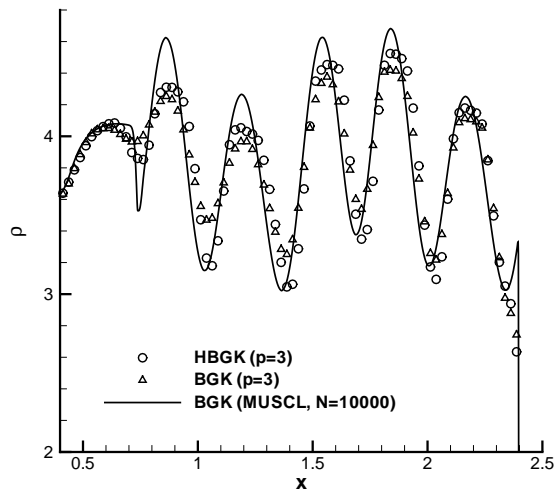


Figure 8: Detailed density distributions calculated by HBGK ($p=3$) and previous 2nd-order BGK scheme ($p=3$).

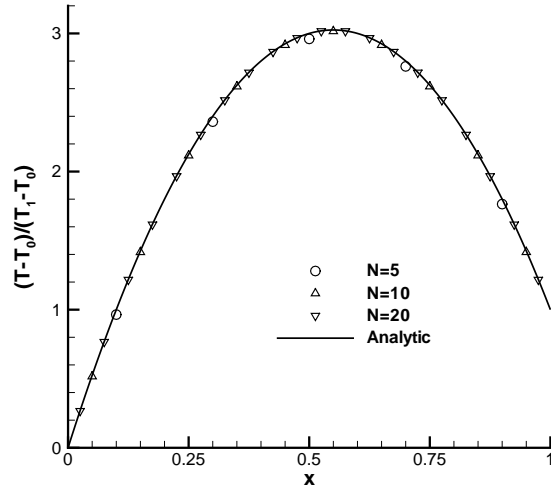


Figure 9: Temperature ration profiles in the Couette flow. The solid line labeled by 'analytic' represents the solution given by Eq. (26). Symbols are computed by HBGK scheme ($p=2$) with different grid numbers.

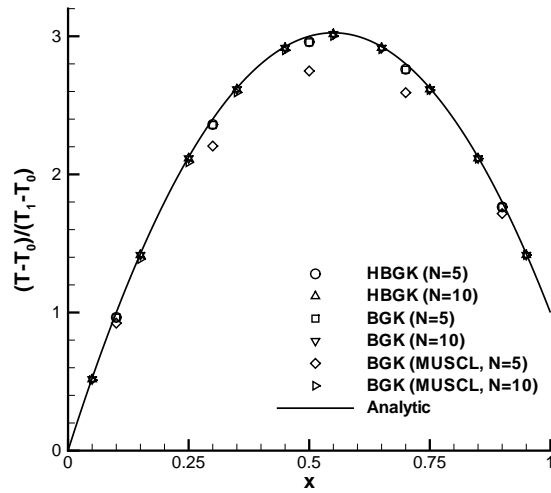


Figure 10: Comparison of temperature profiles in the Couette flow using HBGK ($p=2$), 2nd-order BGK ($p=2$), and 2nd-order BGK (MUSCL) with different grid numbers.

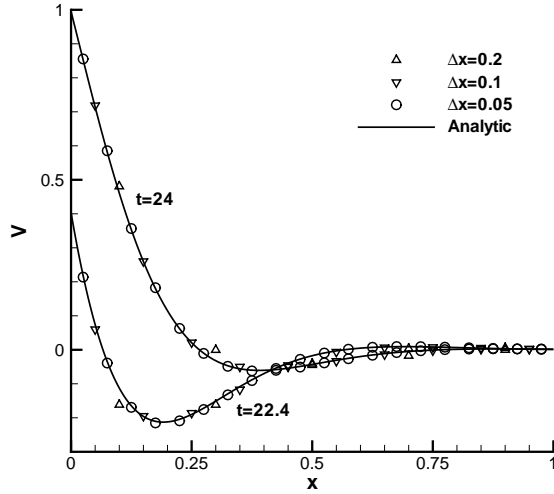


Figure 11: Velocity profiles for flow near an oscillating plate. The solid line labeled by 'analytic' represents the solution given by Eq. (27). Symbols are computed by HBGK scheme ($p=2$) with different grid number.

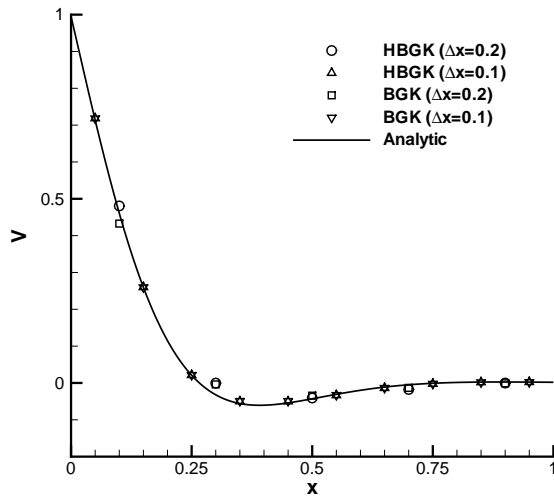


Figure 12: Velocity profiles at $t = 24$ in the oscillating plate flow computed by HBGK ($p=2$) and previous 2nd-order BGK scheme ($p=2$).

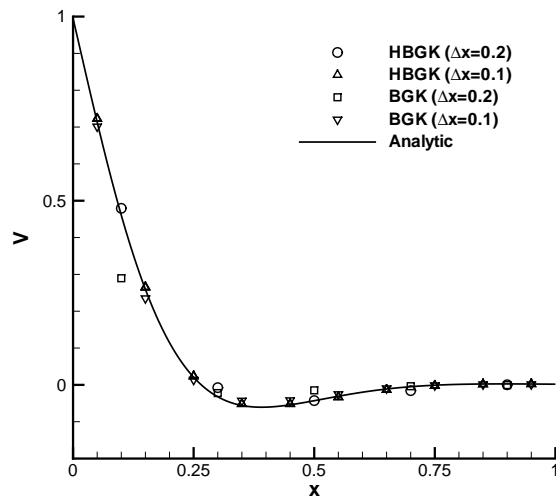


Figure 13: Velocity profiles at $t = 24$ in the oscillating plate flow computed by HBGK ($p=2$) and previous 2nd-order BGK scheme ($p=2$) with CFL number 0.9.